www.sciencemag.org/cgi/content/full/317/5838/653/DC1

Supporting Online Material for

The Source of Saturn's G Ring

Matthew M. Hedman,* Joseph A. Burns, Matthew S. Tiscareno, Carolyn C. Porco,
Geraint H. Jones, Elias Roussos, Norbert Krupp, Chris Paranicas, Sascha Kempf

*To whom correspondence should be addressed. E-mail: mmhedman@astro.cornell.edu

Published 3 August 2007, *Science* **317**, 5838 (2007)
DOI: 10.1126/science.1143964

This PDF file includes:

SOM Text
Figs. S1 to S7
Table S1
References

Supporting Online Material for "The Source of Saturn's G Ring":

Supporting Text:

Image Processing

Casssini images of the G ring were calibrated using the standard pipeline (*S1*), which converts raw data numbers into measurements of *I/F*, the ratio of brightness of the scene to that of a perfect Lambert surface at normal incidence. To account for differences in the viewing geometry, these brightness estimates were then multiplied by μ (the sine of the ring opening angle) to obtain the brightness of the ring viewed at normal incidence, known as the "normal *I/F*".

The appropriate spacecraft and trajectory SPICE kernels were used to geometrically navigate the images. The positions of known stars in the field of view were then used to refine the pointing, and to obtain the equatorial radius and longitude of each pixel in the image. With this information, we azimuthally averaged the signal to produce radial profiles like those shown in Fig. 1, or re-projected the data onto grids in radius and longitude to make maps like that shown in Fig. 4.

The longitudinal profiles shown in Fig. 3 derive from six sequences of images (See Table S1). During each sequence the camera watched material rotate through a certain inertial longitude in the G ring. For most of these sequences, the images were first re-projected onto a grid of radii and (inertial) longitudes, then for each longitude bin we integrated the normalized brightness over orbital radius to obtain the normal equivalent width $\int \mu \, I/F \, dr$. This quantity is used instead of the peak *I/F* value because equivalent width is relatively insensitive to image resolution (*S2*). The integration range is chosen separately for each sequence in order to capture the entire arc signal. A combined profile for each sequence was constructed from the individual image profiles assuming the arc orbits Saturn at a fiducial rate (445.475 ^{0}/day). This final profile consists of the average equivalent width measured within each corotating longitude bin, and the error bars are computed based on the variance of the equivalent-width estimates within each bin. Note that in the 19 Sep 2006 data we also subtract a background level.

The data sets from 30 Oct 2005 and 25 Apr 2006 were processed slightly differently from the others because these sequences were taken at very small ring-opening angles ($<0.5^0$), which meant that the data could not be re-projected onto a radius/longitude grid without significant distortion. For these data sets we obtained a single radial profile of the G ring from each image, and computed an effective longitude for that scan based on the spacecraft position. The equivalent width was then computed for each profile. For the 30 Oct 2005 observations the resulting data are binned in longitude to improve signal-to-noise.

Numerical Simulations

We conducted numerical simulations of 3,830 massless test particles near the Mimas 7:6 CER. Particle orbits about Saturn were evolved under the influence of Mimas as well as eight other saturnian moons, the Sun, and Jupiter. Saturn's J_2 and J_4 harmonic coefficients (*S3*), resulting from the planet's oblateness, were also accounted for. Inter-particle collisions were neglected, due to the G Ring's low optical depth. The integrations were carried out using software based on the Swift package (*S4*-*S6*). The orbits of the massive perturbers were not directly integrated; rather, their positions at each time step were obtained from JPL ephemeris kernels DE414 and SAT252 (*S7*). The test particles were directly integrated for 80 years – 1 Jan 1970 to 1 Jan 2050, the entire length of time available in the ephemerides for the massive perturbers.

Because standard (osculating) orbital elements can behave pathologically under an oblate central mass, varying significantly on orbital timescales, we use epicyclic orbital elements (*S8*-*S11*) to define input parameters and to analyze the simulation outputs, as well as in all discussions below. The simulation code itself uses Cartesian coordinates for input and output.

All particles began with their epicyclic eccentricity and inclination set to zero. Initial epicyclic semi-major axis ranged from 167,472.5 to 167,510.5 km, sampling the phase space surrounding the Mimas 7:6 corotation eccentricity resonance (CER, resonant argument $\varphi_{\mathrm{CER}} = 7\lambda_{\mathrm{Mimas}} - 6\lambda_{\mathrm{arc}} - \varpi_{\mathrm{Mimas}}$), while longitudes covered 0^{o} to 66^{o}, sampling the full phase space around one of the six CER co-rotation sites.

Most simulated particles (2,820) are clearly trapped in the CER, with $|\Delta\varphi_{\mathrm{CER}}| < 150^{\mathrm{o}}$. Confinement in the resonance is effective, with no significant leakage over the 80-year integration.

The dominant period for libration of the semimajor axis is 1273 +/- 3 days (Figure S1b), though the period increases for very loosely bound particles ($|\Delta\varphi_{\mathrm{CER}}| > 130^{\mathrm{o}}$). Also present in the semimajor-axis libration is a long period resulting from Mimas' own motion under its 4:2 resonance with Tethys. This libration, which is slow enough that test particles move adiabatically along with Mimas, has a period of ~72 yr (*S12,S13*) and imparts to resonant test particles an amplitude of ~4 km in semimajor axis. Other weaker frequencies are also present in both librations.

The libration of the resonant argument also has a dominant period of 1273 +/- 3 days for $|\Delta\varphi_{\mathrm{CER}}| < 130^{\mathrm{o}}$. Secondary frequencies are generally different from the secondary frequencies in the semimajor axis, with 596 +/- 3 days being the second-most prominent period.

The width of the resonance is given by the amplitude of the semimajor axis libration, which increases directly with the resonant argument libration amplitude and which is a measure of how tightly bound to the resonance a test particle is. The most loosely bound particles that are still in the resonant phase space have $\Delta a \sim 35$ km (Figure S1a); subtracting the 4 km due to Mimas' 72-year libration gives a resonance width of 31 km.

Since all test particles began in circular coplanar orbits, the eccentricity and inclination forced by outside perturbations can be estimated from the mean values of the epicyclic eccentricity and inclination over the integration's lifetime. More tightly bound particles tend to have lower e and i, with characteristic values being $e \sim 0.001$ (Figure S1c) and $i \sim 0.003^\circ$ (Figure S1d).

The dominant simulated libration period of 1273 days is significantly longer than the interval covered by the currently available observations (743 days). Thus far we have seen the arc run slightly slower than the resonance, beginning slightly ahead of a corotation site and drifting behind it. This can be explained as simply part of a libration cycle; if this is correct, we would expect to discern a turnaround in the next year or two, with the arc speeding up and overtaking the corotation site again.

We can explain the observed radial width of the arc (~250 km) with a combination of the resonance width and the forced eccentricities in our simulations. The resonance width (i.e., the range of semimajor axes among resonant particles) is 31 km; subtracting this from the observed value, we are left to account for ~220 km of radial width. This corresponds to an eccentricity $e \sim 0.0007$ (given the semimajor axis $a \sim 167{,}500$ km), which is consistent with the simulated forced eccentricities (Figure S1c).

LEMMS observations during G-ring crossings

Cassini crossed regions magnetically connected to the G-ring during three orbits, for six total passes inbound and outbound. Figures S2-S5 show despiked time series of count rates in the LEMMS channels E4-E6 with the electron pitch angles observed by the spacecraft (*S14,S15*).

Fig. S2 and S3 show the data from 1 July 2004. The sinusoidal variations in the count rates occur because LEMMS scanned continuously through a range of pitch angles during these observations. These oscillations complicate interpretation of these data, but there is no evidence for a strong absorption in these data. Subtle variations in the electron flux may be present in the data, but they would be considerably weaker than the strong absorption seen in Fig.3.

Fig. S4 shows the data from 14 Apr 2005. There are no absorption signatures visible in either the inbound or outbound data.

Fig. S5 shows the full time series of the 5 Sep 2005 pass. The strong absorption can be seen clearly at ~12:13 UTC. Other shifts in the level are associated with changes in spacecraft orientation. However, the small dip at ~11:58 may represent a second absorption signature. Unfortunately, this occurs during a spacecraft turn, so it is difficult to say whether this feature is really a second microsignature associated with the G ring or its arc.

Despite the evidence for possible variations absorptions on previous crossings, these features are not nearly as strong as that observed at ~12:13 on 5 Sep 2005. Furthermore, Pioneer 11 and Voyager 2 also crossed the G-ring a total of four times and did not record anything peculiar in their energetic electron detectors. The presence of the G-ring therefore cannot explain the sharp electron absorption seen on 5 Sep 2005. Given the proximity of Cassini to the G-ring arc at this time, the additional material contained in this structure is most likely responsible for the electron absorption.

Arc inclination and the absorption signature displacement

Given the elevation of the spacecraft above the ring plane (Fig. S6) and the radial displacements of microsignatures of small and mid-sized satellites (*S15,16*), we interpret the ~3000 km displacement of the 5 Sep 2005 absorption signature relative to the visible arc's location as the result of magnetospheric phenomena. One possible alternative explanation is that the arc moves on an inclined orbit. An inclined orbit could bring the arc to higher (magnetic) latitudes, which in turn means that the arc would thread different field lines that have their equatorial location (L-shell) at larger distance. Therefore the inclination can lead to outward displacements of the arc's electromagnetic imprint, as observed.

Assuming that the arc's inclination is i, then the maximum latitude that the arc can reach is also i. The shape of a field line as a function of latitude in a dipole field is given by $r = L\cos^2\varphi$, where r is the radial distance, L is the equatorial field line distance (L-shell) and φ is the latitude. Using $\varphi=i$, and from observations, $r=167500$ km, and $L=170789$ km, we get that $i \sim 8^0$. Corrections for the fact that the magnetic equator is northwards displaced compared to the kronographic equatorial plane, can lower this not less than 4^0.

Nearly edge-on observations of the G Ring (Images N1524626870-N1524639589, ring-opening angle $\sim 0.07^0$) place an upper limit of ~100 km on the vertical thickness, corresponding to a maximum allowable inclination of 0.02°. This is consistent with the simulated forced inclinations, which are far smaller (Figure S1d). Furthermore, if the entire G ring does derive from the arc, a finite inclination in the arc would produce a finite vertical thickness in the entire ring. Edge-on views of the ring show the visible G ring is less than 200 km thick. The arc's inclination is therefore unlikely to be large enough to explain the arc's displacement.

LEMMS Estimates of the Arc's Mass

This analysis uses procedures described in (*S15*). The electron flux (measured in counts per second or *CPS*) during the outbound 5 Sep 2005 microsignature reached a minimum value CPS_{final} of ~50% the background level outside the microsignature ($CPS_{initial}$) . We can therefore define the following measure of the strength of the absorption:

$$f = -0.5\ln\left(\frac{CPS_{final}}{CPS_{initial}}\right) \sim 0.2 \qquad (1)$$

such that the total column mass of material along the electrons' paths is $K=fR$, where the "range" R is the column mass of material required to attenuate the population of penetrating electrons by a factor of e^2. This range depends only on the electrons' energy and the material. Assuming water ice and 1 MeV electrons, $R \sim 1$ g/cm^2 (*S17*).

The column mass K is related to the arc's total mass M by the following approximate expression (derived from equation (7) in *S18*):

$$M = 0.5\, w\, KVT_b \cos \theta_{eq}, \qquad (1)$$

where θ_{eq}~35^0 is the equatorial pitch angle, $w \sim 250$ km is the radial width of the arc,
T_b is the electron bounce period and V is the bounce-averaged velocity of the electrons relative to the arc, which depend the particle's energy E and θ_{eq} *(S19)*.

Using the above values we get that:

$$M \sim (2*10^6 \text{ cm})\, RVT_b \qquad (3)$$

The remaining terms depend on the electron energy E, so Figure S7 shows M as a function of E. Near 1 MeV M falls to approximately 10^8 kg because at this energy the drift velocity V is close to the keplerian orbital velocity, so electrons can spend a long time passing through the arc, and lower masses are needed to produce a given absorption. At other energies the total mass must be around 10^{10} kg.

Calculation of optical depth profile of the outer G ring:

The optical depth τ of the ring at a given δa away from the arc is given by the integral:

$$\tau = \int \pi s^2\, n(s,\delta a)\, ds, \qquad (4)$$

where s is the particle size and $n(s,\delta a)$ is the differential particle size distribution at a distance δa away from the source region. Assuming the ring is in a steady state, there must be as many particles drifting into a given orbit as drifting out of it. Hence the number flux of particles of size s across a given δa must be the same as the number flux of particles of size s_0 at $\delta a=0$. In other words, $v_a(s,\delta a)\, n(s,\delta a)\, ds = v_a(s_0,0)\, n(s_0,0)\, ds_0$, where v_a is the radial velocity of the particles. Assuming the particle size decays exponentially with distance from the arc like $s=s_o e^{-\delta a/3D}$, then $ds= e^{-\delta a/3D}\, ds_o$. Furthermore, since $v_a = da/dt \propto 1/s$, $v_a(s,\delta a) = v_a(s_0,0)e^{+\delta a/3D}$. The conservation of flux thus requires that $n(s,\delta a) = n(s_0,0)$.

Therefore, $\tau = \int \pi s^2\, n(s,\delta a)\, ds = \int \pi s^2\, n(s_0,0)\, ds = e^{-\delta a/D} \int \pi s_0^2\, n(s_0,0)\, ds_0 = \tau_o e^{-\delta a/D}$.

Supporting Figures:

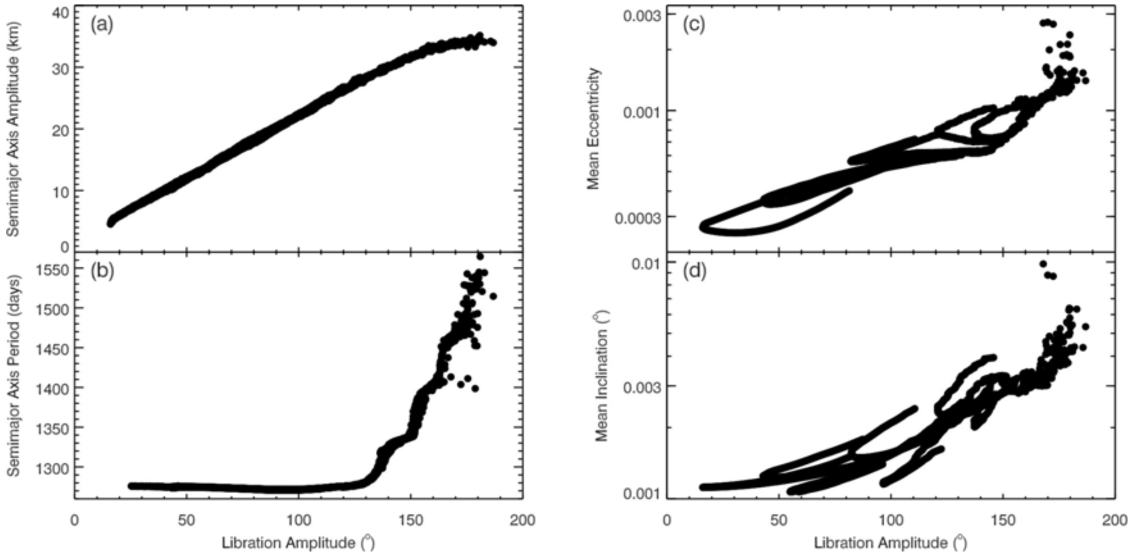

Figure S1: Attributes of simulated resonant particles, plotted against amplitude of resonant argument libration. (a) amplitude of semimajor axis libration, (b) dominant period of semimajor axis libration, (c) mean eccentricity over the 80-year integration, (d) mean inclination over the 80-year integration.

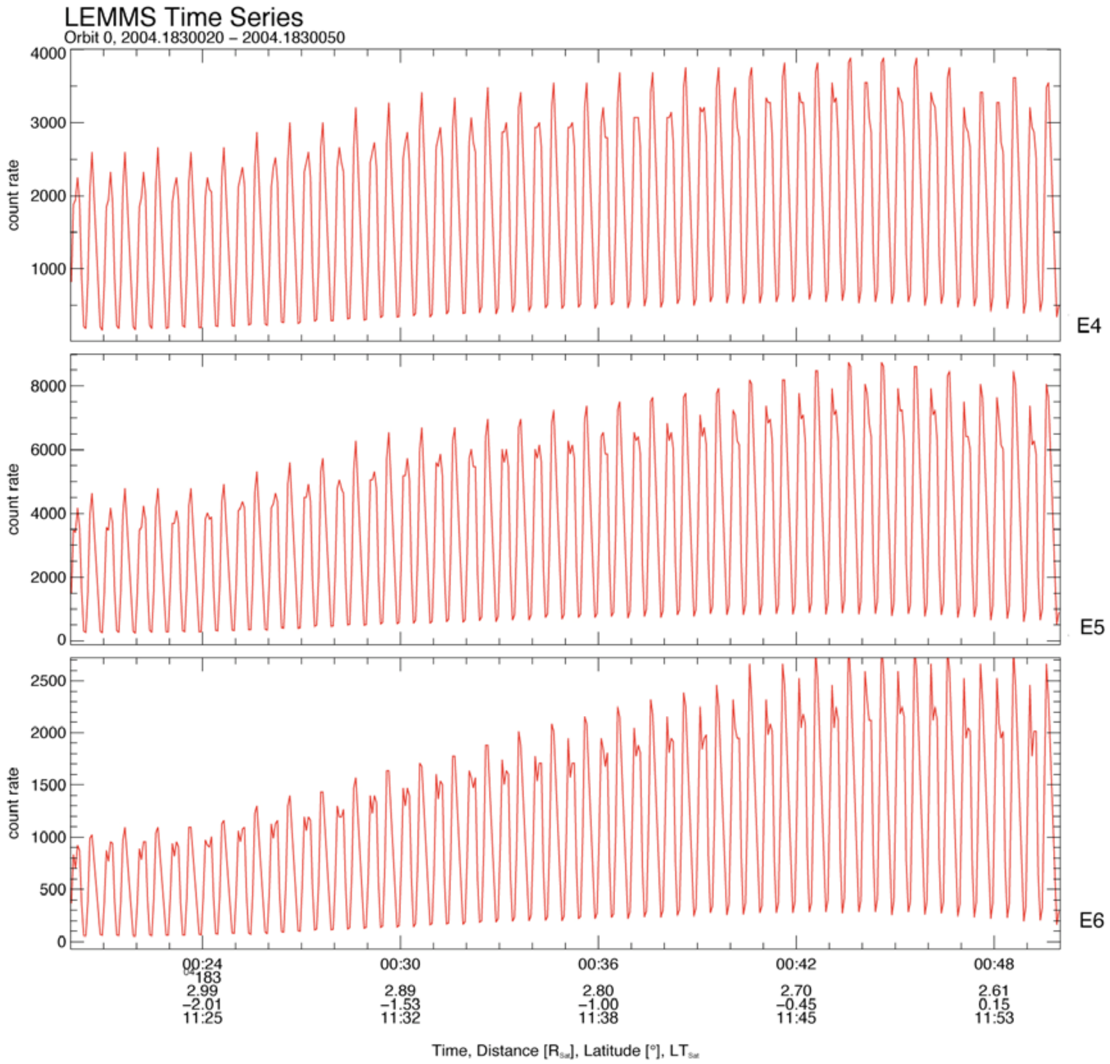

Figure S2: LEMMS data taken during the inbound G-ring crossing of 1 July 2004. Each panel shows the time series in one LEMMS channel. Sinusoidal variations in the fluxes occur because the instrument continuously scanned over a range of pitch angles.

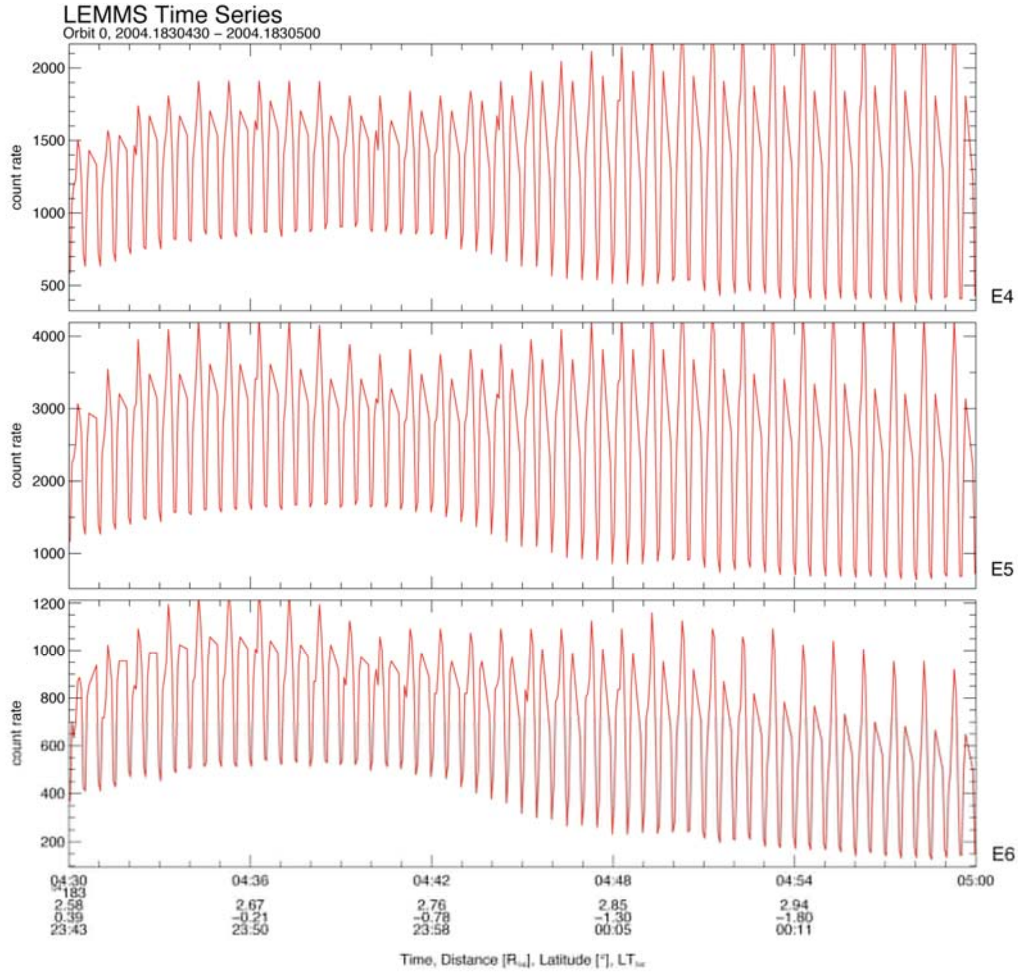

Figure S3: LEMMS data taken during the outbound G-ring crossing of 1 July 2004. Each panel shows the time series in one LEMMS channel. Sinusoidal variations in the fluxes occur because the instrument continuously scanned over a range of pitch angles.

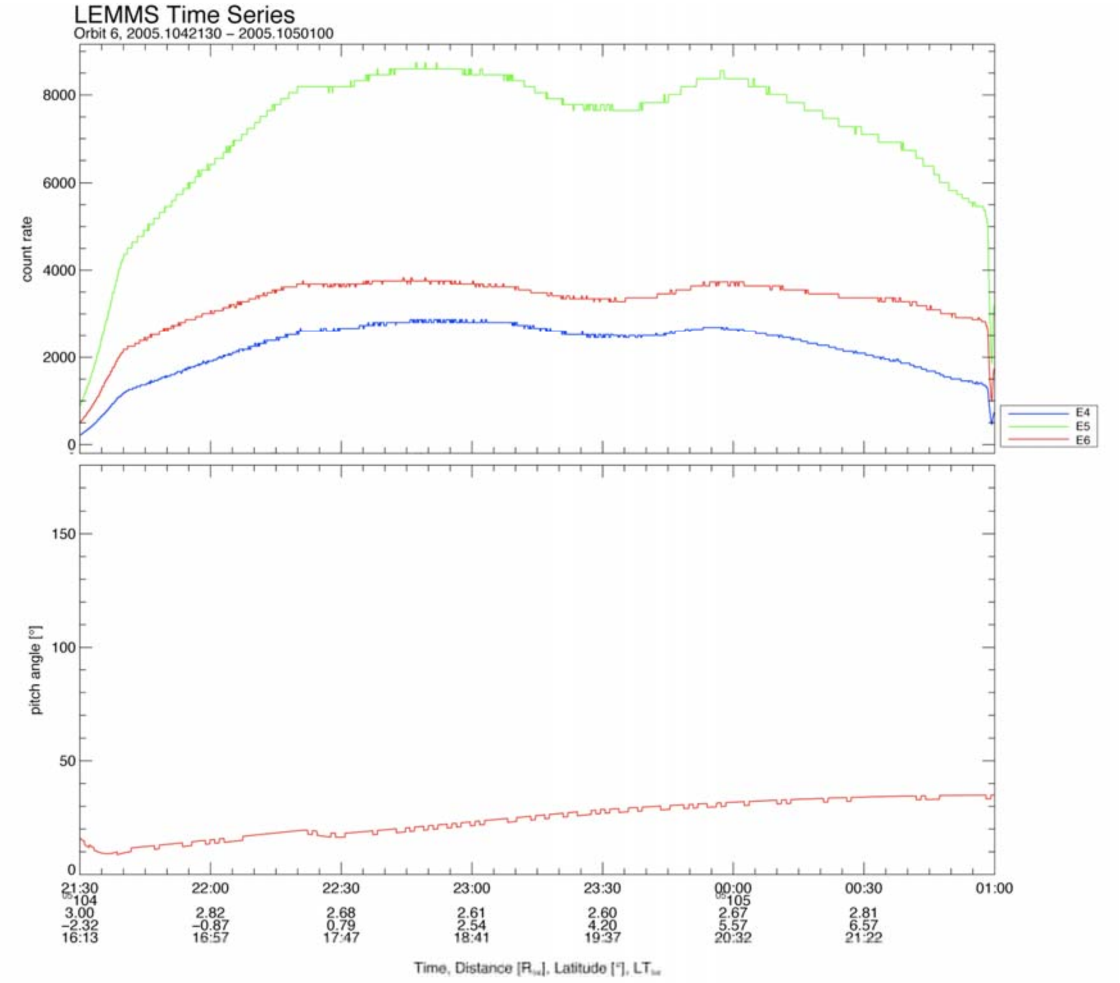

Figure S4: LEMMS data from the G-ring crossing of 14 Apr 2005. Top panel shows the time series of LEMMS channels E4-E6. The bottom panel shows the electron pitch angles observed by LEMMS during this time based on the orientation of the spacecraft. The bottom axis gives the day of year and time during the observation, as well as the spacecraft location in terms of L-shell, latitude and the local time. There is no indication of sharp electron absorptions in these data.

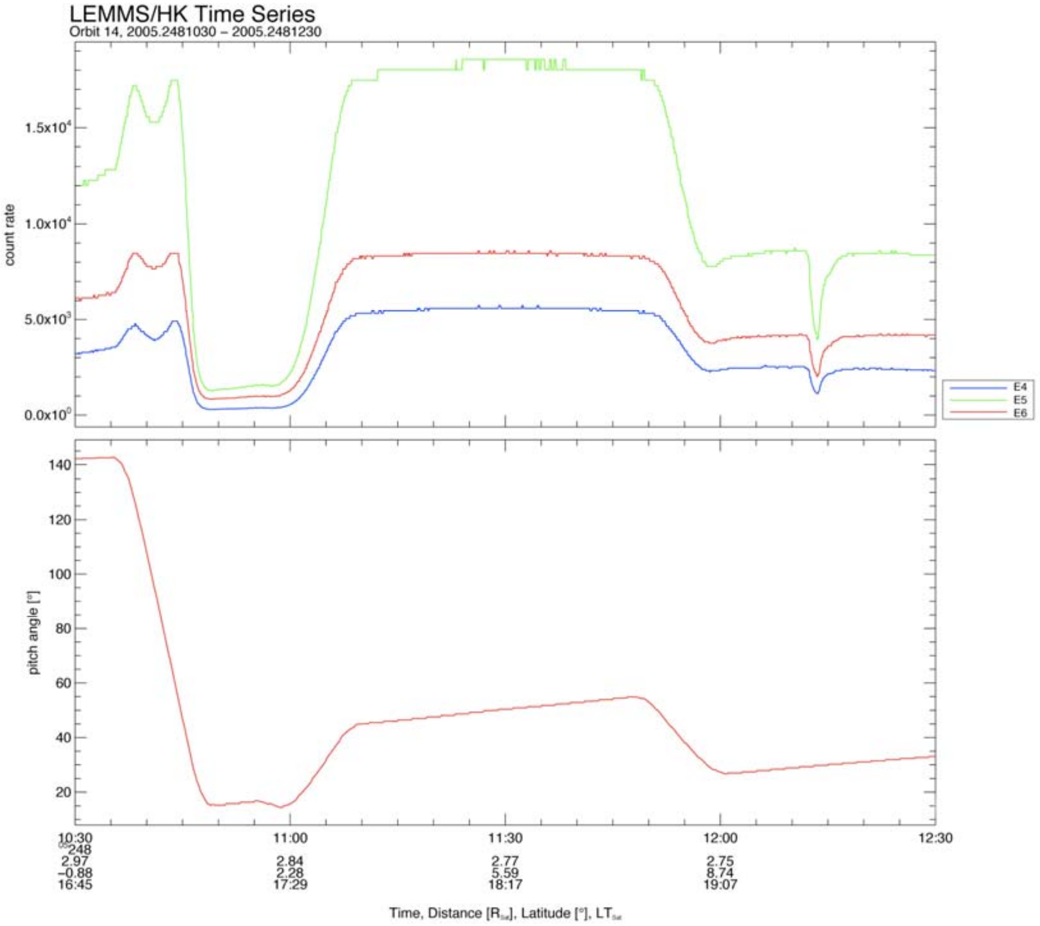

Figure S5: The time series of the LEMMS data in the E4-E6 channels during the periapsis of 5 Sep 2005, along with the electron pitch angles determined by the spacecraft orientation (see Fig. S3). During the plotted time interval, Cassini made a high latitude crossing of the magnetic field lines that thread the G-ring arc and observed electron depletion at ~12:13, during the outbound pass. The corresponding inbound signature, if present, was likely masked by one of the spacecraft re-orientation maneuvers during this period. These changes in LEMMS pointing are primarily responsible for the large changes in count rate and pitch angle coverage. The small flux variation observed between 11:55 and 12:00 may be the best candidate for being an inbound absorption signature by the arc.

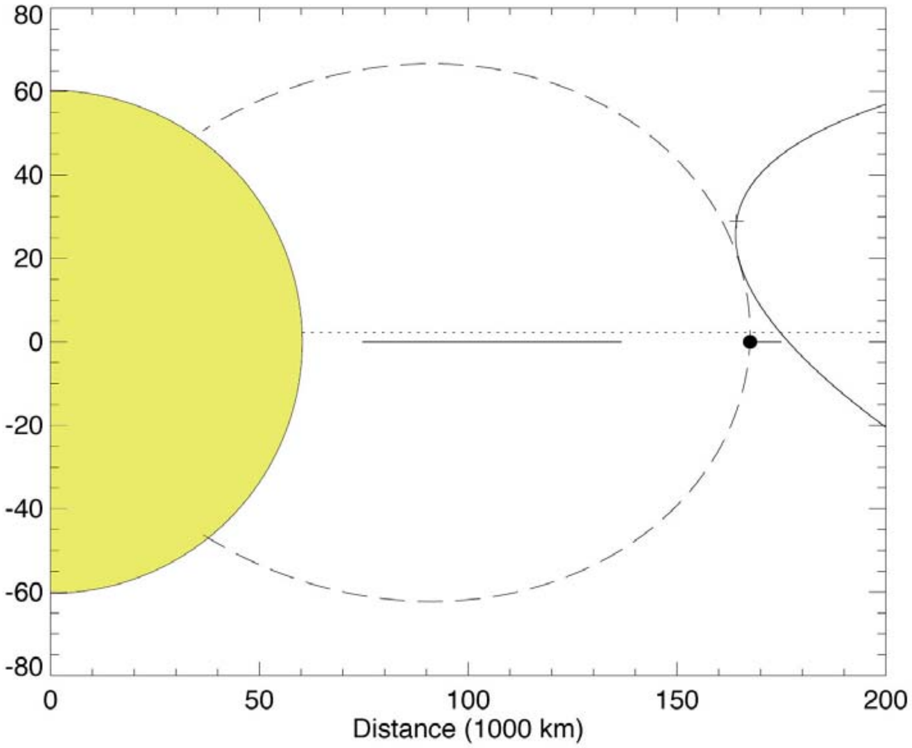

Figure S6: Vertical geometry of Cassini's 5 Sep 2005 passage near the G ring. The yellow sphere represents Saturn, while the horizontal black line represents the main rings (A-C). The position of the arc is marked with the dot. The dotted line indicates the location of the magnetic equator, and the dashed line shows the magnetic field line connected to the arc assuming an unperturbed dipole field. The solid arc shows the track of the Cassini spacecraft, with the position of the deep absorption indicated by the plus sign.

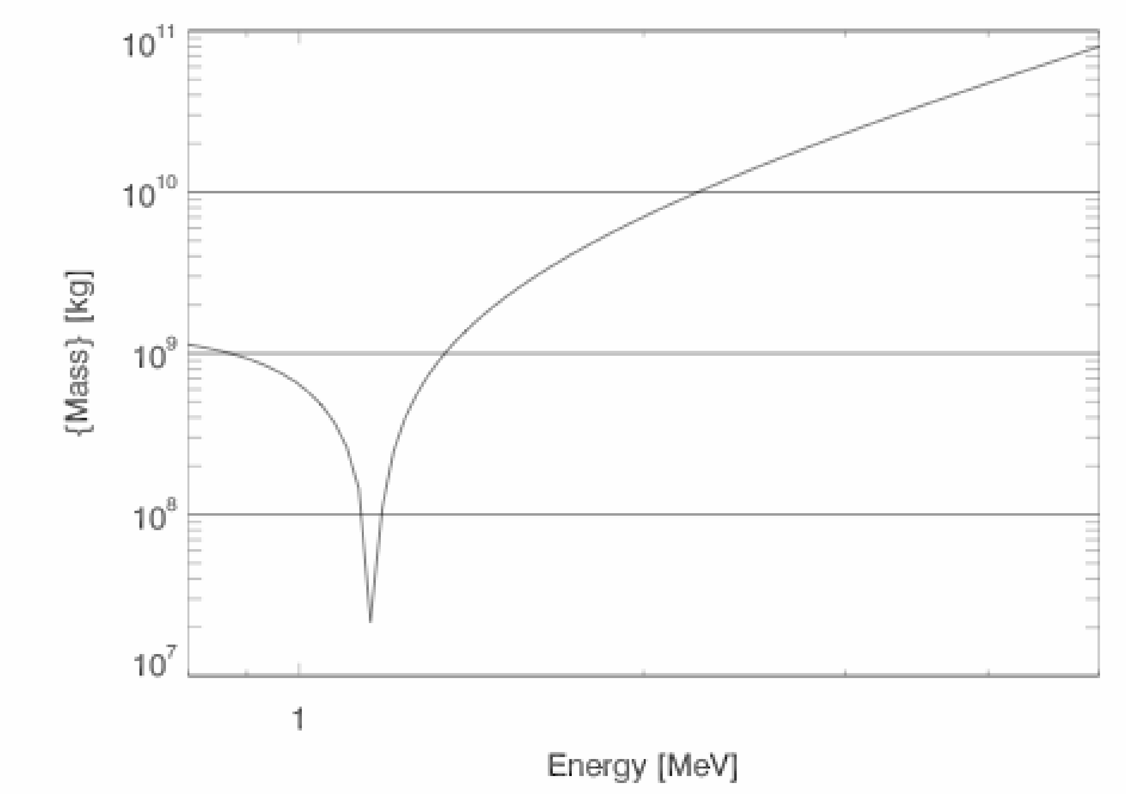

Figure S7: The total arc mass that is required to cause the observed electron absorption, as a function of electron energy.

Supporting Tables:

Table S1: ***ISS observations of G-ring****:*

Observation Date	File names	Ring Opening Angle[a] (degrees)	Phase Angle[b] (degrees)	Radial Resolution (km/pixel)	Range Integrated (km)
06 Sep 2004	N1472855263 N1473631252	16.9	84.0	55	167000-168000
24 May 2005	W1495621314 W1495623920 W1495626500 W1495629054 W1495631634 W1495634240 W1495636820 W1495639374	3.9	85.5	105	166000-169000
30 Oct 2005	N1509387606 through N1509395522 (72 images)	0.3	157.5	5	166000-169000
25 Apr 2006	N1524617785 through N1524648674 (18 images)	0.1	102.8	25	166000-169000
04 Jul 2006	N1530684463 N1530687000 N1530689537	0.7	144.9	25	165500-169500
19 Sep 2006	N1537362584 through N1537431998 (70 images)	10.0	162.5	15	166000-168500

[a] Angle between the ring plane and the light ray entering the camera from the ring.

[b] Angle between the incident ray from the sun and reflected ray from the ring.

Supporting References and Notes

S1. C. C. Porco *et al., Space Science Reviews* **115**, 363 (2004).
S2. M.R. Showalter, J.N. Cuzzi, *Icarus* **103** 124 (1993).
S3. R. A. Jacobson *et al.*, *Astron. J.* **132**, 2520 (2006).
S4. Available online http://www.boulder.swri.edu/hal/swift.html.
S5. Wisdom, M. Holman, *Astron. J.* **102**, 1528 (1991).
S6. M. J. Duncan, H. F. Levison, M. H. Lee, *Astron. J.* **116**, 2067 (1998).
S7. Available online ftp://naif.jpl.nasa.gov/pub/naif/generic_kernels/spk
S8. N. Borderies, P.-Y. Longaretti, *Icarus* **72,** 593 (1987).
S9. P.-Y. Longaretti, N. Borderies, *Icarus* **94**, 165 (1991).
S10. N. Borderies-Rappaport, P.-Y. Longaretti, *Icarus* **107**, 129 (1994).
S11. S. Renner, B. Sicardy, *Celest. Mech. Dyn. Astron*. **94**, 237 (2006).
S12. Y. Kozai, *Ann. Tokyo Astron. Obs*. **5**, 73 (1957).
S13.R. A. Jacobson, J. Spitale, C. C. Porco, W. M. Owen, *Astron. J.* **132**, 711 (2006).
S14. S. M. Krimigis *et al., Space Science Reviews* **114**, 233 (2004).
S15. Roussos, E. *et al., Icarus* accepted manuscript (2007).
S16. G. H. Jones *et al., Science* **311**, 1412 (2006).
S17. http://physics.nist.gov/PhysRefData/Star/Text/ESTAR.html
S18. J. N. Cuzzi, J. A. Burns *Icarus* **74** 284 (1988).
S19. M. F. Thomsen, J. A. Van Allen , *J. Geophys. Res.* **85** A115831 (1980)